nature physics

ARTICLES

PUBLISHED ONLINE: 27 JUNE 2016 | DOI: 10.1038/NPHYS3806

Klein tunnelling and electron trapping in nanometre-scale graphene quantum dots

Christopher Gutiérrez[1], Lola Brown[2], Cheol-Joo Kim[2], Jiwoong Park[2,3] and Abhay N. Pasupathy[1]*

Relativistic fermions that are incident on a high potential barrier can pass through unimpeded, a striking phenomenon termed the 'Klein paradox' in quantum electrodynamics. Electrostatic potential barriers in graphene provide a solid-state analogue to realize this phenomenon. Here, we use scanning tunnelling microscopy to directly probe the transmission of electrons through sharp circular potential wells in graphene created by substrate engineering. We find that electrons in this geometry display quasi-bound states where the electron is trapped for a finite time before escaping via Klein tunnelling. We show that the continuum Dirac equation can be successfully used to model the energies and wavefunctions of these quasi-bound states down to atomic dimensions. We demonstrate that by tuning the geometry of the barrier it is possible to trap particular energies and angular momentum states with increased efficiency, showing that atomic-scale electrostatic potentials can be used to engineer quantum transport through graphene.

According to the Dirac equation, massless fermions pass unimpeded through arbitrary potential barriers at normal incidence, a phenomenon termed Klein tunnelling[1,2]. The band structure of graphene, a single layer of carbon atoms in a honeycomb lattice, provides a solid-state analogue to this effect[3–9] which is uniquely amenable to direct scanned probe measurements. Klein tunnelling arises from two fundamental properties of graphene. First, the spectrum of states is gapless[10]—regardless of the energy of the incident electron, quantum states always exist across the barrier for the electron to transition into. Second, due to the honeycomb structure of the graphene lattice, the wavefunctions of graphene are two-component spinors with amplitudes on each of the sublattices[10]. Conservation of this sublattice isospin degree of freedom in the tunnelling process is directly responsible for the high transmissibility of electrons at normal incidence[3]. At oblique incidence, however, both reflection and transmission can occur at the barrier, with reflection becoming dominant at large incidence angles[3,4]. The unique nature of Klein tunnelling and the related phenomenon of negative refraction has been proposed as a building block to steer, and even confine, electrons by the use of cleverly designed barriers[5,6,11]. Signatures of these phenomena have been seen in transport[12–14] experiments on graphene devices incorporating electrostatic barriers. However, direct imaging of the wavefunctions at potential boundaries and atomic-scale verification of the predictions of Klein tunnelling has not yet been achieved, and is the subject of this Letter.

The basic ideas for Klein tunnelling discussed above can also be applied to the case of a circular quantum well in graphene. In the well-known case of two-dimensional electron gases (2DEG) in semiconductor heterostructures, such quantum wells form bound eigenstates that can be used to completely trap an electron, creating highly tunable quantum dots[15]. For circular quantum wells, the eigenstates also have well-defined angular momentum. In the case of graphene, the lack of a band gap makes complete trapping of an electron impossible in such a graphene quantum dot (GQD). However, for sufficiently large GQDs, we can consider the edge of the dot to be similar to a one-dimensional barrier. Electrons incident at large angles will be reflected from the edge of the barrier with high probability, and can continue to bounce around many times before finally making their escape. This basic intuition says that electrons that have high angular momentum can be quasi-bound inside the GQD, whereas those with small angular momentum escape quickly[16–21]. The quasi-bound states give rise to resonances of finite width (corresponding to a finite trapping time) in the local density of states (LDOS) within the GQD, which can be detected by local probes. Indeed, a recent scanning tunnelling microscopy (STM) experiment detected precisely such resonances in the LDOS, and the results were explained consistently using the Dirac physics of electrons in graphene[21]. In that experiment, however, the scanning tip itself was responsible for the trapping potential, making direct imaging of the electronic wavefunctions and verification of the predictions of Klein tunnelling impossible. In this work, we use STM to probe nanometre-sized n–p–n GQDs with boundaries that are sharp (∼1 nm) compared to the typical wavelengths of the electrons being probed. Using spectroscopic imaging, we directly image the wavefunctions of quasi-bound states in this geometry. We show that the spatial structure, energetic positions and trapping times of the quasi-bound states can be used to directly verify the predictions of Klein tunnelling and the spinor nature of graphene wavefunctions.

Our GQDs are produced by substrate engineering that leads to different potential energies inside and outside the dot, as shown in the cartoon in Fig. 1a. Briefly, our samples are produced by the epitaxial growth of graphene on single-crystalline copper (111) foils by a special high-temperature growth process that leads to a reconstruction of the copper surface below the graphene film[22,23]. During this growth, almost all of the copper substrate below the graphene film is in the (111) orientation, accompanied by a long-wavelength spiral reconstruction[23], as shown in the STM topograph in Supplementary Fig. 1b (details of the reconstruction are described in the Supplementary Information). However, rare, nanometre-sized quasi-circular patches of the copper substrate do not display the spiral reconstruction. Two such patches can be seen in the STM topograph in Fig. 1b. Importantly, the graphene sheet is perfectly continuous and free of defects across the entire area of Fig. 1b, as shown in the atomically resolved STM

[1]Department of Physics, Columbia University, New York, New York 10027, USA. [2]Department of Chemistry and Chemical Biology, Cornell University, Ithaca, New York 14853, USA. [3]Kavli Institute at Cornell for Nanoscale Science, Ithaca, New York 14853, USA. *e-mail: apn2108@columbia.edu

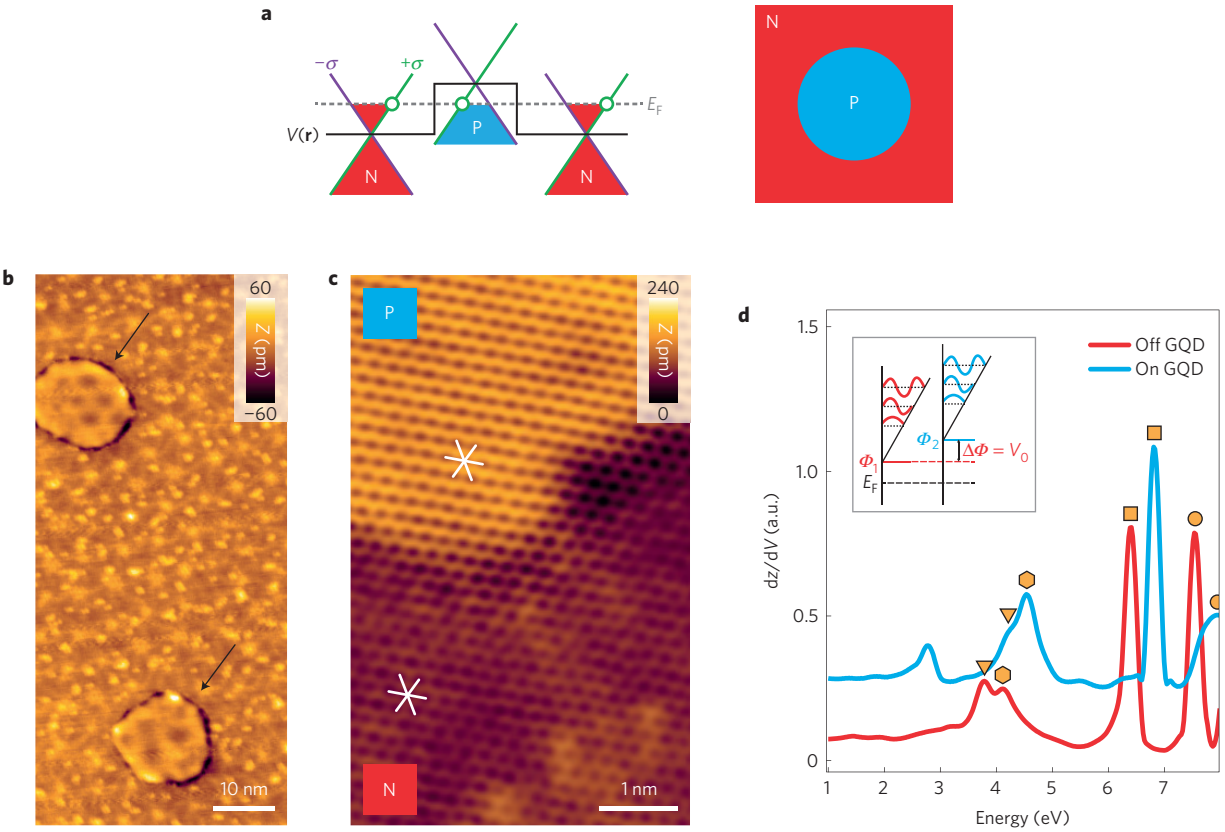

Figure 1 | Klein tunnelling in a continuous graphene sheet. a, Left panel: Schematic of Klein tunnelling across a circular n–p–n junction. The potential $V(\mathbf{r})$ sends an incident conduction electron (green circle) into the valence band while conserving the sublattice isospin $\sigma+$ (green line). Right panel: overhead view of the circular potential. **b**, Large-area STM topograph of the epitaxial graphene–Cu(111) surface ($V_b = -2$ V, $I = 2$ pA). The majority of the copper surface undergoes a spiral reconstruction, although rare, near-circular patches of copper do not reconstruct. The bright, atomic protrusions (~50–80 pm tall) peppering the surface are vacancies in the Cu(111) substrate. Black arrows point to areas of the Cu(111) that are not epitaxially matched to graphene, and display randomly oriented Moire patterns (see Supplementary Information). These patches act as graphene quantum dots (GQDs). **c**, Atomically resolved STM image across the boundary of one such patch, showing the perfect continuity of the graphene lattice (white lines) ($V_b = -10$ mV, $I = 150$ pA). **d**, Field-emission resonance (FER) peaks recorded via dz/dV spectroscopy on (blue) and off (red) a GQD. The +0.42 eV shift in the FER peaks is seen in four separate pairs of peaks (like symbols). The unpaired peak at ~2.75 eV appears only on GQDs. (Setpoint condition: $V_s = 1$ V, $I_s = 150$ pA.) Inset: energy diagram of the FER peak shift process.

topograph in Fig. 1c. We note that the contrast in the apparent STM heights in Fig. 1b,c primarily stems from variations in the LDOS (further STM images at other biases are shown in the Supplementary Information).

The two different areas of the copper surface produce surface potentials that dope the graphene sheet differently. Indeed, atomic rearrangements of the surface (for example, surface reconstructions) can affect the local work function[24,25], $\Phi(\mathbf{r})$, and thus alter the local potential landscape underneath graphene. These differences in the local work function can be measured very precisely by recording the energy shift in field-emission resonance (FER) peaks (also known as Gundlach states)[26–29]. In this measurement, the height of the STM tip, $z(V)$, is recorded as a function of the tunnelling bias voltage, V_b. At tunnelling energies above the sample work function, resonant standing-wave states of a triangular potential become electronically accessible in the tip-sample region (Fig. 1d, inset), giving rise to peaks in the dz/dV spectrum. Changes in the work function are then reflected in the shifts of the FER peaks. Figure 1d displays dz/dV spectra recorded on and off a quasi-circular patch. A positive shift of $V_0 = +0.42$ eV is measured for four separate sets of resonant peaks (Fig. 1d, shaded symbols). As both photoemission spectroscopy[22] and dI/dV measurements (Fig. 2a) on the majority reconstructed surface place the graphene Dirac point at $E_D^{OUT} \approx -0.28$ eV, indicating n-doping, this measured positive shift on the copper patches would move the Dirac point to $E_D^{IN} \approx +0.14$ eV, indicating p-doping (see Supplementary Information for further discussion). Thus, the quasi-circular patches act as n–p–n junctions in the graphene above (Fig. 1a). For this reason we refer to these patches as graphene quantum dots. Since the dots have slightly asymmetric shapes, we define their average radii by $R = \sqrt{A/\pi}$, where A is the area of the GQD as measured from STM topographs. The radii of the GQDs range from ~2.5 nm (about 10 lattice constants) to ~8 nm (about 32 lattice constants). The transition from the n to the p region of the copper occurs over approximately four lattice constants (~1 nm), which is much shorter than the Fermi wavelength (29.5 nm in the p-doped region and 14.8 nm in the n-doped region). Thus, this system provides a unique way to measure the effect of sharp and strong potentials in graphene at the near-atomic scale.

Using dI/dV spectroscopy we can probe the LDOS inside and outside the GQD. Outside the GQD, the LDOS spectrum (green curve, Fig. 2a) is smooth, with a minimum observed at $E_D^{OUT} \approx -0.28$ eV. In contrast, LDOS measurements taken inside the quantum wells reveal a series of resonance peaks at negative energies (that is, in the GQD valence band, Fig. 1a). A representative set of dI/dV curves is shown in Fig. 2a, with the locations where they were obtained shown in the inset. The intensity and energy width of the peaks is seen to depend on the radial distance from the

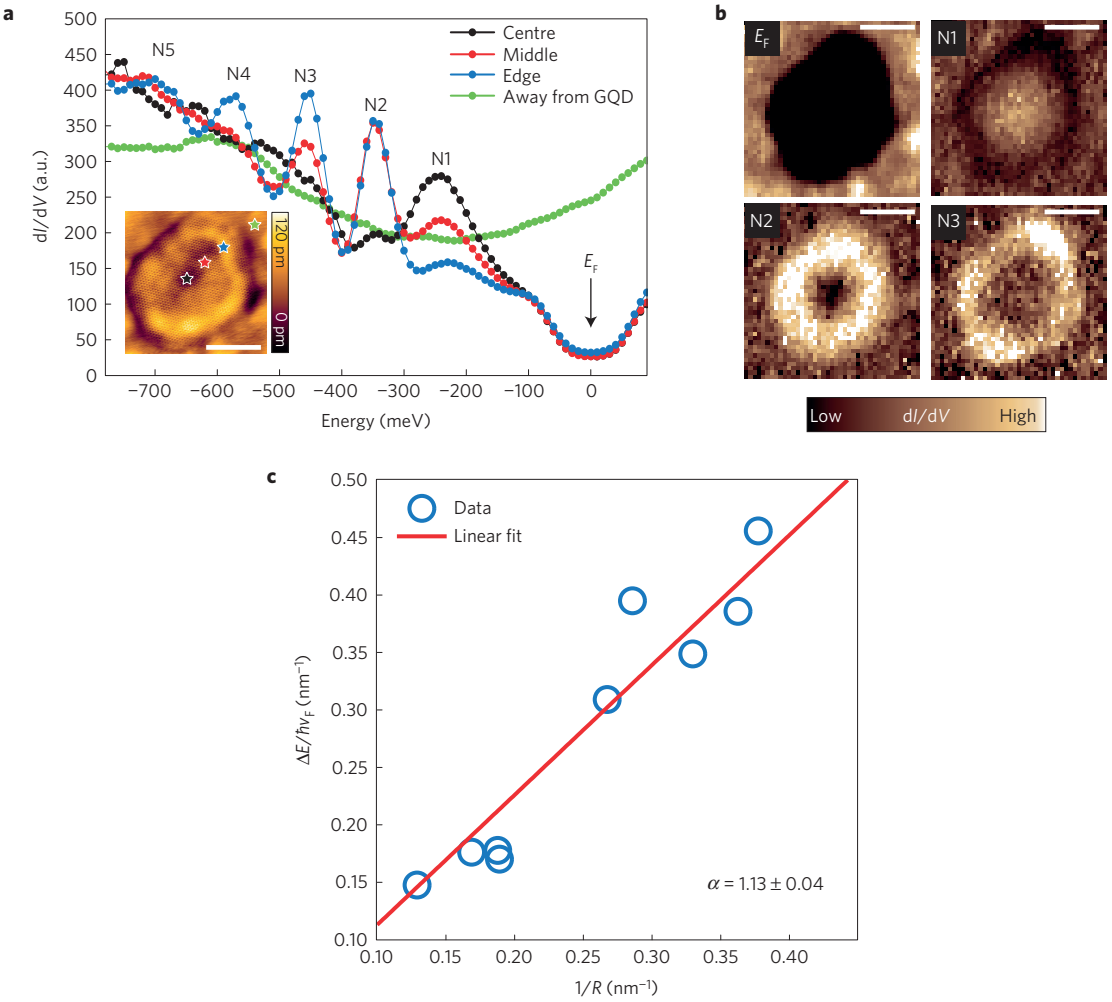

Figure 2 | Quasi-bound states in a graphene quantum dot. a, dI/dV spectra taken at different locations on and off a typical GQD shown in the inset. We see a sequence of resonances on the GQD whose intensity depends on the location of the measurement. These resonances are observed only below the Fermi energy, and are not seen outside the GQD (green curve). Furthermore, on the GQD we observe a graphene inelastic tunnelling channel[34,35] at $E \approx \pm 67$ mV. **b**, Spectroscopic images at the Fermi energy and at the location of the first three peaks in the dI/dV spectra observed on the GQD. The first resonance has a spatial structure with a maximum at the centre of the GQD, whereas successive resonances have maxima that shift progressively outwards from the centre towards the edge of the GQD. Scale bars in **a**,**b**, 5 nm. (Setpoint condition: $V_s = -0.8$ V, $I_s = 200$ pA.) **c**, Plot of the mean energy spacing as a function of inverse radius for GQDs that displayed at least three resonant modes. The data is described well by a linear fit which gives a dimensionless proportionality factor (see text) of $\alpha = 1.13 \pm 0.04$.

centre. We can visualize these variations in the LDOS with dI/dV mapping, wherein we record spectra at each pixel position on the GQD. Figure 2b displays LDOS($\mathbf{r}$,E) slices at the energies marked in Fig. 2a. The lowest resonance displays strong intensity near the centre of the GQD. Higher resonances display maxima that are progressively closer to the edge of the GQD. A similar progression of wavefunctions is observed in all GQDs (with different sizes) measured in this study. Furthermore, for all the GQDs measured (15 in total), no resonant states were found in the conduction band (see Supplementary Information).

The spectra and wavefunctions described above constitute our main experimental results. This is the first reported visualization of quasi-bound Dirac electrons at sharp, step-potential n–p junctions. Previous STM experiments have studied finite-sized patches of chemical vapour deposition (CVD)-grown GQDs on the surface of Ir(111)[30–33]. We stress that the origin of the quantized states in these prior studies is due to quantum size effects from the finite extent of the graphene flake. We will show that this is very different from the resonant states we observe due to Klein tunnelling in a continuous graphene sheet.

The energies and the shapes of the wavefunctions seen in GQDs above are in agreement with the description of confinement of Dirac electrons in the GQDs. First, the resonances are observed only below the GQD Dirac point, $E_D^{IN} \approx 0.14$ eV—that is, in the valence band of graphene (Fig. 1a, central Dirac cone). This is in accord with the sign of the potential well, where the inside of the well is at higher potential energy than the outside. Such a well forms a trapping potential for holes, but not for electrons. Second, for Dirac electrons in a circular geometry the lowest-lying resonant states for each angular momentum are spaced linearly. The level spacing is related to the GQD radius by $\Delta E \approx \alpha \hbar v_F / R$, where α is a dimensionless constant of order unity, $\hbar$ is Planck's constant divided by 2π, and $v_F \approx 10^6$ m s^{-1} is the Fermi velocity. We indeed observe a linear dispersion of energies in our GQDs, as shown in Fig. 2c, where we extract a value of $\alpha = 1.13 \pm 0.04$ from a linear fit. Third, the progression of wavefunctions seen in the GQDs matches our expectation for particle-in-a-box states in a circular two-dimensional quantum well. For particles inside such a quantum well, the radial part of the wavefunction is described by Bessel functions of the first kind. The lowest of these functions features a maximum in the centre

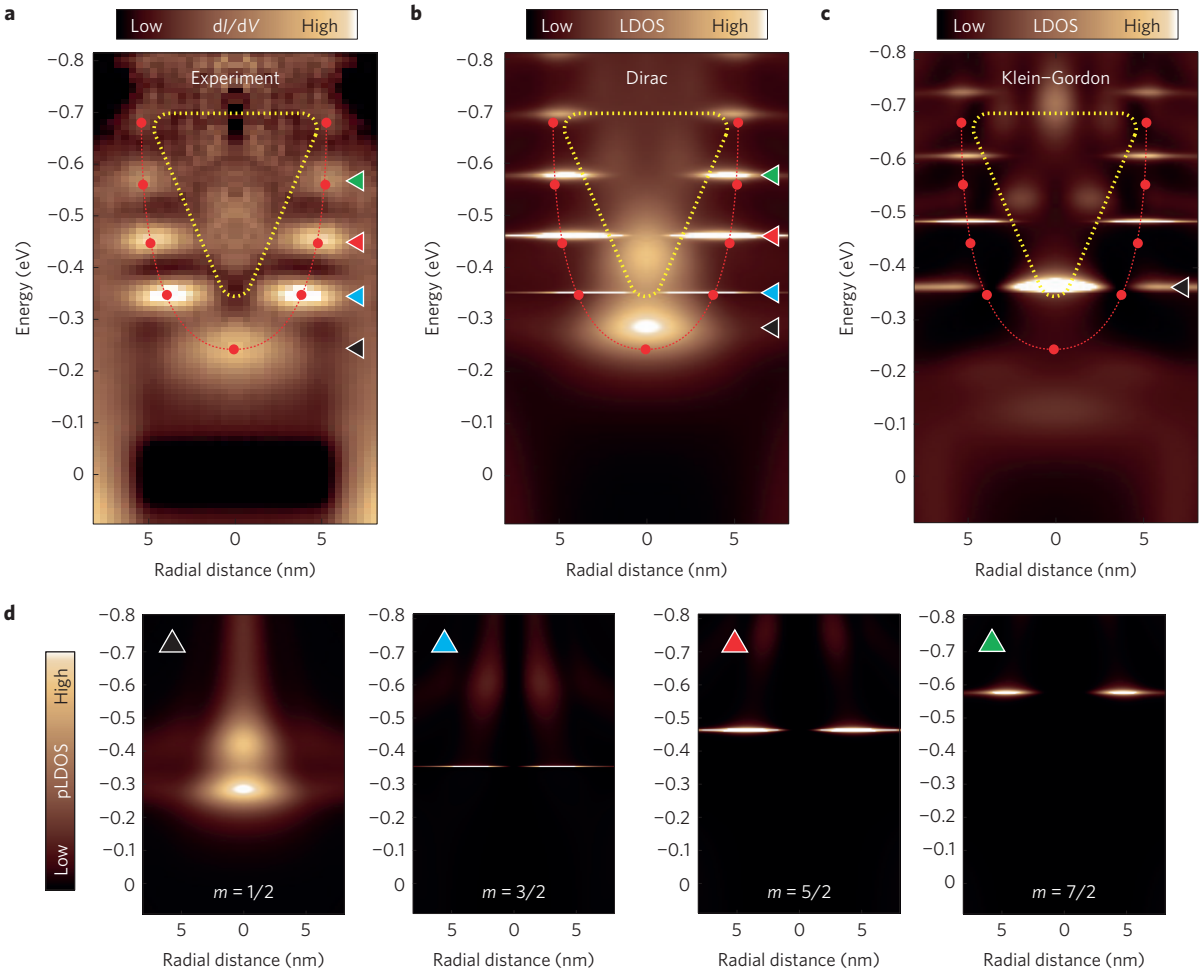

Figure 3 | Spectrum of quasi-bound states of a GQD. a, Radially averaged dI/dV spectroscopic map of the GQD in Fig. 2. The energy location of the first four states is indicated by coloured arrows. The spatial maximum of each state is denoted by a red dot, and the dashed line is a guide to the eye. Additional fine spatial structure is seen at high energy within the region bounded by the dashed yellow line. (Setpoint condition: $V_s = -0.8$ V, $I_s = 200$ pA.) **b**, Solution to the continuum Dirac equation for a circular geometry with the same GQD radius and barrier height as seen in the experiment. The coloured triangles indicate the energy position of each quasi-bound state. The experimental locations of the maxima from **a** (red dots and dashed red line) are overlaid on the calculation for comparison. We see a close match between theory and experiment both for the main resonance peaks, as well as for the more subtle structure seen within the dashed yellow line. **c**, Solution to the Klein–Gordon equation for the same geometry. The ground state (black triangle) and higher states are not well matched to experiment, and fine details within the yellow dashed line also do not match experiment well. **d**, Decomposition of the Dirac solution in **b** into the first four angular momentum channels. We see that the density of states near each main resonance stems primarily from a single angular momentum mode.

of the GQD, and successive wavefunctions have radial maxima that progress towards the edges. This is exactly the behaviour observed in our GQDs (Fig. 2b). Finally, we note that the resonances we observe have energy widths that are larger than the temperature and instrumentation broadening of our spectra (Methods). This is also consistent with the intuition that these resonances are not true bound states of the GQDs, but are instead states where the holes are trapped for a finite time τ, leading to a resonant width $\delta\varepsilon = \hbar/\tau$, where $\delta\varepsilon$ is the full-width at half-maximum (FWHM) of the resonant mode in dI/dV curves[16,17]. We also note that, in general, the electrons in graphene have a non-zero probability to transition into the surface of the copper substrate, which would lead to a decrease in trapping time and wider resonances.

The analogy to particle-in-a-box states gives us a basic understanding of the spectra and spectroscopic images seen on GQDs. In what follows, we develop a quantitative comparison to the predictions of Klein tunnelling. A useful way to visualize this trapping of relativistic electrons is to radially average the dI/dV map data around the centre of the GQD. We can then view the full spectrum through a cross-sectional slice of the GQD, as shown in Fig. 3a. This type of plot increases the signal-to-noise and allows one to view both the spectral width of the resonant modes (along the vertical energy axis) as well as the peak radial distance of the resonant mode (along the horizontal radial axis). It is clear from this plot that the higher resonant modes shift from the centre of the GQD and move outwards. For this particular GQD, it is apparent that the first mode (N1) has a much broader spectral and spatial width than higher modes, indicating weaker confinement. To compare with theory, we first note that although it is sharp on the length scale of the electron Fermi wavelength, the measured potential barrier is reasonably smooth on the scale of the lattice constant of graphene. This in turn implies that intervalley scattering (which requires a true point scatterer) is weak in these dots, which is also confirmed by our STM imaging (see Supplementary Information for more details). We therefore neglect valley mixing in what follows, and solve the (continuum model) Dirac equation in the presence of a circular potential step given by $V(r) = V_0\Theta(R - r)$, where V_0 is a constant and $\Theta(R - r)$ is the Heaviside step function. Since the

potential is cylindrically symmetric, we look for spinor solutions of the form

$$\psi_m(r,\varphi) = e^{im\varphi}\begin{pmatrix}\chi_A(r)e^{-i\varphi/2}\\ i\chi_B(r)e^{i\varphi/2}\end{pmatrix} \quad (1)$$

where the total angular momentum quantum number m is an odd half-integer, and $\chi_A(r)$, $\chi_B(r)$ are the radial-dependent wavefunctions on the graphene A-, B-sublattices, respectively. The total wavefunction, $\Psi(\mathbf{r},E)$, is then a linear combination of these ψ_m, where E is the electron energy, and $\mathrm{LDOS}(\mathbf{r},E) \propto |\Psi(\mathbf{r},E)|^2$. (Details of the calculation can be found in the Supplementary Information.) The results for a perfectly circular potential barrier are shown in Fig. 3b. The theoretical calculation shows a progression of resonant states that move outwards from the centre of the GQD, capturing the essence of Klein tunnelling and matching well with experiment (Fig. 3a). Interestingly, the close match (± 0.01 eV) of the positions of the resonant modes in experiment and theory reveals that the expected confinement in the measured GQD is not strongly perturbed by the irregular shape and/or edge termination (zigzag or armchair) of the measured GQD. The exception is the N1 state, which theory predicts to appear at a lower energy (by $\sim$0.04 eV). This discrepancy may be due to the asymmetric shape of the experimental GQD in Fig. 2, which we model as a perfect circle in our calculations.

The good correspondence between theory from the continuum Dirac equation and experiment for the energies and wavefunctions gives us confidence to explore further the implications of Klein tunnelling in the GQD. To decipher the orbital character of the features in the total LDOS in Fig. 3a,b, we calculated the contributions due to individual angular momenta modes m (Supplementary Information). Figure 3d displays the partial local density of states, $\mathrm{pLDOS}(m,\mathbf{r},E)$, for the lowest four angular momenta resonant states from theory. We see from these images that the main resonance peaks observed in experiment occur at integer steps of the angular momentum quantum number m. Apart from the main resonance peak, each pLDOS map shows a sequence of resonant states at higher energies, which are in general weaker and broader than the main resonance. These additional resonances appear as subtle features near the centre of the GQD, and can also be seen in the experiment in Fig. 3a (within the triangular region defined by the dashed lines, see also Supplementary Information), giving us further confidence in the continuum Dirac model.

The linear spacing of energy levels (Fig. 2c and Supplementary Fig. 3, Supplementary Information) is a direct consequence of the linear energy spectrum of Dirac electrons. We can now ask how the second prerequisite for Klein tunnelling—that is, the sublattice isospin degree of freedom—is manifested in the results. We find that the spinor structure of the graphene wavefunctions has observable consequences both for the resonant energies and wavefunctions of the quasi-bound states in our experiment. To elucidate this, consider a hypothetical graphene electron that is stripped of its spinor structure and instead has a scalar wavefunction. Such a particle would mimic a massless, spinless particle, and thus could be described by the Klein–Gordon equation[9], which has effectively described finite-sized GQD islands[30–33]. In similar fashion to our previous Dirac calculations, we solve the Klein–Gordon equation in the presence of a potential step (Supplementary Information) for the GQD in Fig. 2. The results (Fig. 3c) correctly predict a linear progression of quasi-bound states, but their energies (and spatial geometry) do not match experiment (Fig. 3a). Therefore, the Dirac description is crucial to evaluating the correct spectrum of quasi-bound states in GQDs.

The effectiveness of the potential barrier to trap relativistic electrons can be measured by fitting the widths of the resonant peaks found in $\mathrm{d}I/\mathrm{d}V$. The trapping time, τ, is related to the peak

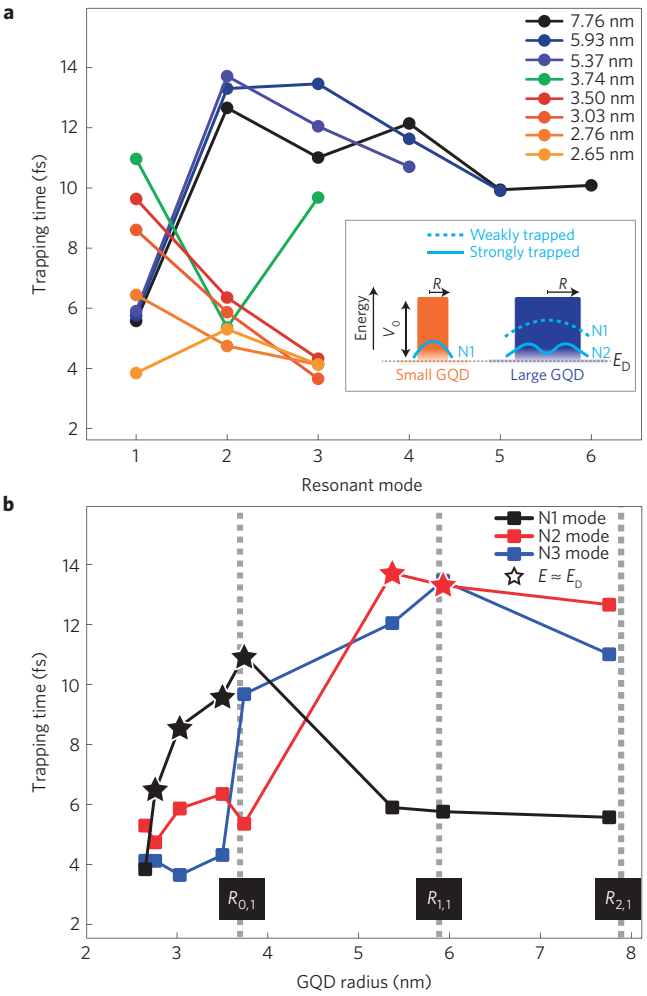

Figure 4 | Trapping times in quasi-bound states. a, Trapping times measured from inverse peak widths of the first few quasi-bound states for GQDs of different radii. In general, smaller (larger) GQDs are better at trapping the N1 (N2) resonant state, as shown in the inset diagram. **b**, Trapping times in **a** plotted as a function of GQD radius. At resonant energies close to the Dirac point, $E_n \approx E_D^{\mathrm{out}} = -0.28$ eV (shown as star symbols), the resonance condition (equation (25) Supplementary Information) yields maximum trapping at specific values of the GQD radii (shown as dashed lines) given by $R_{n,i} = \hbar v_F x_{n,i}/V_0$, where $x_{n,i}$ is the ith zero of the nth Bessel function.

width via $\tau = \hbar/\delta\varepsilon$. Figure 4a displays the results for eight GQDs of different radii. This graph shows that the trapping time is a strong function of both the mode number as well as the size of the GQD. For the larger radii ($r_{\mathrm{avg}} > 5$ nm) the general trend is that of a dramatic increase in the trapping time from the N1 state to the higher states. On the other hand, the smaller radii ($r_{\mathrm{avg}} < 5$ nm) show better trapping for the N1 mode and worse trapping for higher modes. We can plot the same data shown in Fig. 4a as a function of the size of the GQD for each resonance mode. The plot in Fig. 4b shows that, for each mode, there is an optimum GQD radius that best traps that mode. These observations can be simply explained when we consider the two primary influences on trapping. First, due to Klein tunnelling, one expects improved confinement with incident angle[3,4]. This would imply that the higher angular momentum modes are trapped better. On the other hand, the energy of the nth trapped state goes approximately as $E_n \sim \hbar v_F n/R$, as shown in Fig. 2c. Thus, as the GQD gets smaller, the energies of the higher resonant states become larger than the barrier height, leading

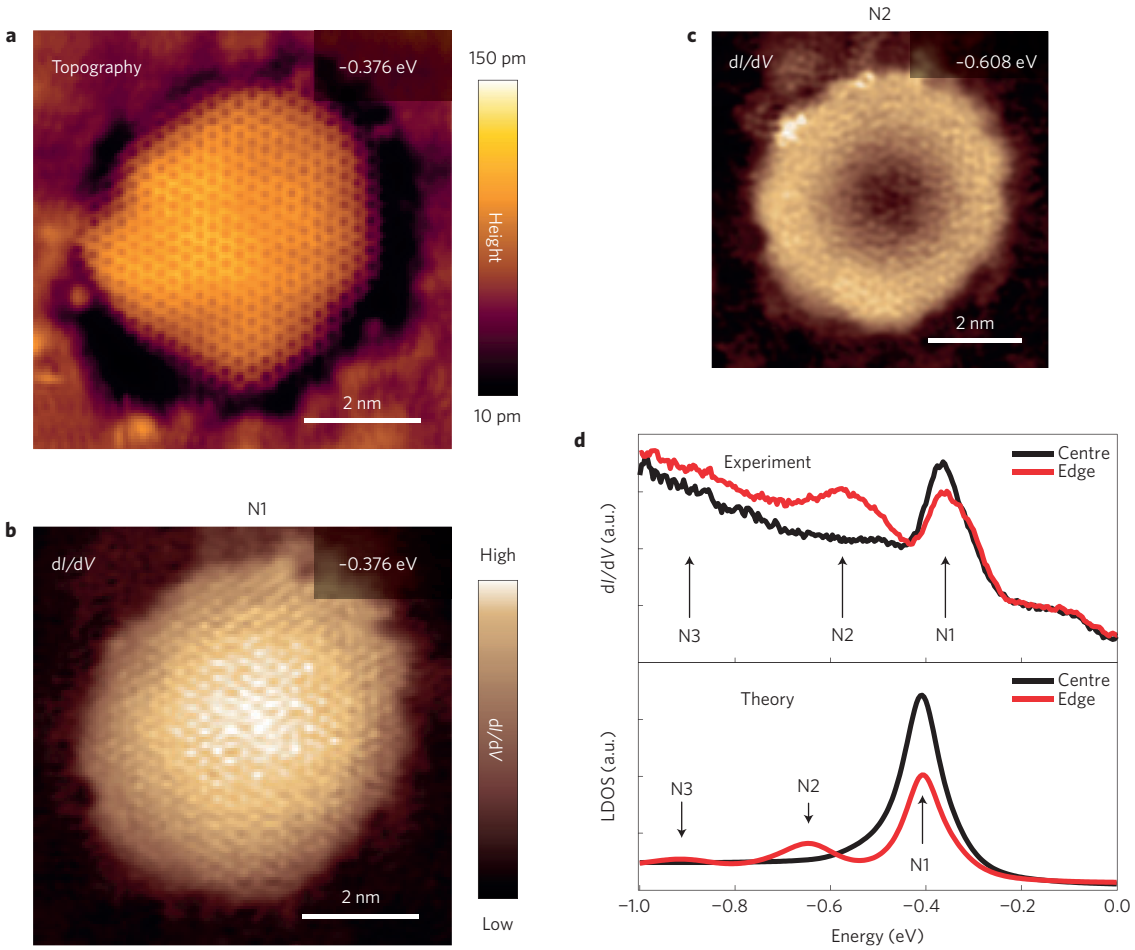

Figure 5 | Atomic-scale GQDs and sublattice symmetry breaking. a, Topographic image of a $R \approx 2.76$ nm GQD, clearly showing the graphene honeycomb lattice. **b**,**c**, Atomically resolved spectroscopic dI/dV images of the first two quasi-bound states. A close examination of the N1 mode in **b** and comparison to the simultaneously acquired topography in **a** shows that the sublattice isospin symmetry is broken inside the GQD, giving rise to the triangular rather than honeycomb spatial structure. (For **a**–**c**, $I = 150$ pA.) **d**, Comparison between the experimental and calculated LDOS spectra from Dirac theory for this GQD, showing that the continuum Dirac equation continues to provide an excellent description even for atomically sized GQDs. (Setpoint condition: $V_s = -1$ V, $I_s = 100$ pA.)

to a loss of trapping efficiency. The net behaviour of the trapping times can be thus be understood as a balance between these two opposing influences.

For a sharp potential, maximum trapping is predicted to occur when two conditions are met (see equation (25) of the Supplementary Information). The first is that the quasi-bound state in question has a resonant energy close to the outside Dirac point[16,17], $E_n \approx E_D^{OUT}$ (star symbols, Fig. 4b). The second condition is that the GQD radius takes on particular values given by $R_{n,i} = \hbar v_F x_{n,i}/V_0$, where $x_{n,i}$ is the ith zero of the nth Bessel function, satisfying $J_n(x_{n,i}) = 0$, for integer $i \geq 1$ (ref. 17). These special radii are displayed as dashed lines in Fig. 4b. Indeed, our curves show that the trapping time peaks when the resonant energies are close (± 0.03 eV) to the Dirac point and coincide with the special GQD radii, confirming the theoretical predictions for electron trapping in step potentials[16,17]. These results show that by precisely tailoring the shape and strength of the quantum well one could create designer GQDs for trapping specific geometric wavefunctions for suitably long timescales.

All of the results above show that the behaviour of electrons in our graphene quantum dots is well approximated by the properties of the continuum Dirac equation. We can probe whether the discrete lattice of graphene is important to understanding the results by studying GQDs with small dimensions. Shown in Fig. 5a is an STM topograph of a GQD with size $R \approx 2.76$ nm (approximately 11 lattice constants of graphene), among the smallest sizes we observe experimentally. In this GQD, we continue to measure quasi-bound states, the lowest two of which are shown in Fig. 5b,c. Figure 5d shows the measured experimental spectra on this GQD and a comparison to the continuum Dirac model applied to this case. Surprisingly, we see that the continuum Dirac equation continues to provide an excellent description of the electronic structure down to these length scales, correctly capturing both the energies and the widths of the quasi-bound resonances. Incidentally, we observe a strong breaking of the sublattice symmetry in the lowest (N1) quasi-bound state structure (as evidenced by the triangular rather than the honeycomb structure observed in the LDOS), the experimental origin of which is currently unknown (see Supplementary Information for further discussion).

Our results show that Dirac electrons can be locally confined within nanoscale regions of a much larger, continuous sheet of graphene. By controlling the potential size and depth, we have shown that it is possible to confine specific energies and angular momentum modes all the way to the volt scale in graphene. Creating a coupled array of such potentials would then allow us to strongly modify the transport and optical properties of native graphene to yield new quantum electronic and optical functionality with a performance extending to the infrared frequency range,

of primary importance to optical communications. Whereas traditional electrostatic gating is difficult to implement at these size scales, substrate engineering provides a facile route to achieve this in practice.

Note added in proof: After acceptance of this paper, we became aware of a related manuscript (ref. 36) showing similar results to this work.

Methods

Methods, including statements of data availability and any associated accession codes and references, are available in the online version of this paper.

Received 10 February 2016; accepted 25 May 2016; published online 27 June 2016

References

1. Klein, O. Die Reflexion von Elektronen an einem Potentialsprung nach der relativistischen Dynamik von Dirac. *Z. Phys.* **53,** 157–165 (1929).
2. Dombey, N. & Calogeracos, A. Seventy years of the Klein paradox. *Phys. Rep.* **315,** 41–58 (1999).
3. Katsnelson, M. I., Novoselov, K. S. & Geim, A. K. Chiral tunnelling and the Klein paradox in graphene. *Nature Phys.* **2,** 620–625 (2006).
4. Cheianov, V. V. & Fal'ko, V. I. Selective transmission of Dirac electrons and ballistic magnetoresistance of n–p junctions in graphene. *Phys. Rev. B* **74,** 041403 (2006).
5. Pereira, J. M., Mlinar, V., Peeters, F. M. & Vasilopoulos, P. Confined states and direction-dependent transmission in graphene quantum wells. *Phys. Rev. B* **74,** 045424 (2006).
6. Cheianov, V. V., Fal'ko, V. & Altshuler, B. L. The focusing of electron flow and a Veselago lens in graphene pn junctions. *Science* **315,** 1252–1255 (2007).
7. Shytov, A. V., Katsnelson, M. I. & Levitov, L. S. Atomic collapse and quasi-Rydberg states in graphene. *Phys. Rev. Lett.* **99,** 246802 (2007).
8. Shytov, A. V., Rudner, M. S. & Levitov, L. S. Klein backscattering and Fabry–Pérot interference in graphene heterojunctions. *Phys. Rev. Lett.* **101,** 156804 (2008).
9. Barbier, M., Peeters, F. M., Vasilopoulos, P. & Pereira, J. M. Dirac and Klein–Gordon particles in one-dimensional periodic potentials. *Phys. Rev. B* **77,** 115446 (2008).
10. Castro Neto, A. H., Guinea, F., Peres, N. M. R., Novoselov, K. S. & Geim, A. K. The electronic properties of graphene. *Rev. Mod. Phys.* **81,** 109–162 (2009).
11. Vakil, A. & Engheta, N. Transformation optics using graphene. *Science* **332,** 1291–1294 (2011).
12. Young, A. F. & Kim, P. Quantum interference and Klein tunnelling in graphene heterojunctions. *Nature Phys.* **5,** 222–226 (2009).
13. Stander, N., Huard, B. & Goldhaber-Gordon, D. Evidence for Klein tunneling in graphene p–n junctions. *Phys. Rev. Lett.* **102,** 026807 (2009).
14. Lee, G.-H., Park, G.-H. & Lee, H.-J. Observation of negative refraction of Dirac fermions in graphene. *Nature Phys.* **11,** 925–929 (2015).
15. Hanson, R., Kouwenhoven, L. P., Petta, J. R., Tarucha, S. & Vandersypen, L. M. K. Spins in few-electron quantum dots. *Rev. Mod. Phys.* **79,** 1217–1265 (2007).
16. Matulis, A. & Peeters, F. M. Quasibound states of quantum dots in single and bilayer graphene. *Phys. Rev. B* **77,** 115423 (2008).
17. Hewageegana, P. & Apalkov, V. Electron localization in graphene quantum dots. *Phys. Rev. B* **77,** 245426 (2008).
18. Bardarson, J. H., Titov, M. & Brouwer, P. W. Electrostatic confinement of electrons in an integrable graphene quantum dot. *Phys. Rev. Lett.* **102,** 226803 (2009).
19. Heinisch, R. L., Bronold, F. X. & Fehske, H. Mie scattering analog in graphene: lensing, particle confinement, and depletion of Klein tunneling. *Phys. Rev. B* **87,** 155409 (2013).
20. Schulz, C., Heinisch, R. L. & Fehske, H. Electron flow in circular graphene quantum dots. *Quantum. Matter* **4,** 346–351 (2015).
21. Zhao, Y. *et al*. Creating and probing electron whispering-gallery modes in graphene. *Science* **348,** 672–675 (2015).
22. Brown, L. *et al*. Polycrystalline graphene with single crystalline electronic structure. *Nano Lett.* **14,** 5706–5711 (2014).
23. Gutiérrez, C. *et al*. Imaging chiral symmetry breaking from Kekulé bond order in graphene. *Nature Phys.* http://dx.doi.org/10.1038/nphys3776 (2016).
24. Sandl, P. & Bertel, E. Surface states, local bonding, and surface reconstruction: Na on Cu (110). *Surf. Sci.* **302,** L325–L330 (1994).
25. Memmel, N. Monitoring and modifying properties of metal surfaces by electronic surface states. *Surf. Sci. Rep.* **32,** 91–163 (1998).
26. Lin, C. L. *et al*. Manifestation of work function difference in high order Gundlach oscillation. *Phys. Rev. Lett.* **99,** 216103 (2007).
27. Borca, B. *et al*. Potential energy landscape for hot electrons in periodically nanostructured graphene. *Phys. Rev. Lett.* **105,** 036804 (2010).
28. Pauly, C., Grob, M., Pezzotta, M., Pratzer, M. & Morgenstern, M. Gundlach oscillations and Coulomb blockade of Co nanoislands on MgO/Mo(100) investigated by scanning tunneling spectroscopy at 300 K. *Phys. Rev. B* **81,** 125446 (2010).
29. Chang, H. W., Wu, B. F., Yao, Y. D., Su, W. B. & Chang, C. S. Co nanoislands on Au (111) and Cu (111) surfaces studied by scanning tunneling microscopy and spectroscopy. *J. Nanosci. Nanotech.* **10,** 4663–4666 (2010).
30. Phark, S.-h. *et al*. Direct observation of electron confinement in epitaxial graphene nanoislands. *ACS Nano* **5,** 8162–8166 (2011).
31. Hämäläinen, S. K. *et al*. Quantum-confined electronic states in atomically well-defined graphene nanostructures. *Phys. Rev. Lett.* **107,** 236803 (2011).
32. Subramaniam, D. *et al*. Wave-function mapping of graphene quantum dots with soft confinement. *Phys. Rev. Lett.* **108,** 046801 (2012).
33. Jolie, W. *et al*. Confinement of Dirac electrons in graphene quantum dots. *Phys. Rev. B* **89,** 155435 (2014).
34. Zhang, Y. *et al*. Giant phonon-induced conductance in scanning tunnelling spectroscopy of gate-tunable graphene. *Nature Phys.* **4,** 627–630 (2008).
35. Natterer, F. D. *et al*. Strong asymmetric charge carrier dependence in inelastic electron tunneling spectroscopy of graphene phonons. *Phys. Rev. Lett.* **114,** 245502 (2015).
36. Lee, J. *et al*. Imaging electrostatically confined Dirac fermions in graphene quantum dots. *Nature Phys.* http://dx.doi.org/10.1038/nphys3805 (2016).

Acknowledgements

We thank I. Aleiner for helpful discussions. Work at Columbia is supported by the Office of Naval Research (award number N00014-14-1-0501, C.G.) and by the Nanoelectronics Research Corporation (NERC), a wholly owned subsidiary of the Semiconductor Research Corporation (SRC), through the Institute for Nanoelectronics Discovery and Exploration (INDEX) (A.N.P.). Support for microscopy measurements is provided by the Air Force Office of Scientific Research (AFOSR) (award number FA9550-11-1-0010, A.N.P.) and by the NSF through the Columbia Center for Precision Assembly of Superstratic and Superatomic Solids (DMR-1420634, A.N.P.). Work at Cornell University is supported by the NSF through the Cornell Center for Materials Research (NSF DMR-1120296). Additional funding was provided by AFOSR (FA9550-16-1-0106, FA2386-13-1-4118) and the Nano Material Technology Development Program through the National Research Foundation of Korea (NRF) funded by the Ministry of Science, ICT, and Future Planning (2012M3A7B4049887).

Author contributions

C.G. performed and analysed all STM measurements and theory calculations. L.B. and C.-J.K. performed CVD growth of graphene samples. J.P. supervised the CVD sample growth. A.N.P. supervised STM measurements. All authors participated in writing the manuscript.

Additional information

Supplementary information is available in the online version of the paper. Reprints and permissions information is available online at www.nature.com/reprints. Correspondence and requests for materials should be addressed to A.N.

Competing financial interests

The authors declare no competing financial interests.

Methods

Epitaxial graphene–Cu(111) foil samples were grown *ex situ* by CVD following a recipe reported previously[22]. CVD graphene samples were annealed in an ultrahigh vacuum chamber at 400 °C for ∼12 h to clean the surface before STM measurements. Scanning tunnelling spectroscopy (STS) data were recorded by standard lock-in detection using a modulation voltage of $V_{rms} = 10$ mV with STM tips that were first calibrated on a Au(111) bulk single crystal. All measurements were performed at 78 K.

Data availability. The data that support the plots within this paper and other findings of this study are available from the corresponding author on reasonable request.